Self-templating Faceted and Spongy Single-Crystal ZnO Nanorods: Resistive Switching and Enhanced Piezoresponse

Alberto Quintana [a*], *Andrés Gómez* [b*], *Maria Dolors Baró* [a], *Santiago Suriñach* [a], *Eva Pellicer* [a], *Jordi Sort* [ac*]

[a] Departament de Física, Facultat de Ciències, Universitat Autònoma de Barcelona, E-08193 Bellaterra, Spain

[b] Institut de Ciència de Materials de Barcelona (ICMAB-CSIC), Campus UAB, E-08193 Cerdanyola del Vallès, Barcelona, Spain

[c] Institució Catalana de Recerca i Estudis Avançats (ICREA), Pg. Lluís Companys 23, 08010 Barcelona, Spain

Keywords: Spongy Nanorods, Faceted Nanorods, ZnO, Resistive Switching, Piezoelectricity

Highlights

- The large area synthesis of faceted and spongy self-standing ZnO single-crystal nanorods is shown.
- Enhanced piezoelectric properties are exhibited by the synthesized nanorods.

- Resistive switching properties have been evaluated in both faceted and spongy nanorods.

Abstract

A template-free, cost-effective, hydrothermal procedure is used to synthesize large areas of either *faceted* or *spongy* self-standing *single-crystalline* ZnO nanorods (NRds) from electrodeposited Zn films. The morphology of the NRds (faceted *versus* spongy) can be easily adjusted by simply varying the electrodeposition parameters of the parent Zn film. The obtained NRds exhibit an enhanced piezoelectric response (compared to bulk ZnO) and resistive switching properties which depend on their intrinsic morphology. This combination of properties together with the simplicity of the synthetic approach is particularly appealing for the fabrication of large arrays of nanosensors, nanoactuators and other applications that could benefit from an enhanced surface area in single-crystalline semiconductors.

1. Introduction

Materials' properties can be often enhanced by introducing porosity or surface roughness to their structure. This approach has successfully been used to boost a widespread range of technological applications, mainly in chemistry, not existing or poorly efficient in conventional fully-dense films and bulk materials. Catalysis and gas sensing are among the conventional fields that benefit from porous or loosely packed (i.e., spongy) structures since the increased surface area provides more catalytic active sites for the reactants and faster kinetics [1]. While spongy and nanoporous materials have been extensively studied from a chemical point of view, some of the physical properties of these types of materials (e.g., piezoelectricity or resistive switching) have

been much less investigated. Nonetheless, the advantages of nanoporous materials in engineering applications like resistive random access memories (RRAM) or strain actuators have become obvious in recent years [2-4]. Hence, it is important that the physical properties of fully dense materials are also maintained or even improved when the microstructure is made porous. Actually, in piezoelectric materials, nanoporosity allows circumventing the detrimental effects of the clamping with the substrate, while it can also promote stabilization of certain crystallographic phases with enhanced piezoelectric response [5].

Another approach to enhance the properties of materials is to scale down their physical dimensions [6,7]. Since the discovery of single-wall carbon nanotubes [8], lots of efforts have been made to produce 1D nanostructures (wires, rods, tubes,…) consisting of other elements and compounds, such as ZnO [9]. These 1D nanostructures can exhibit a better resolution in piezoelectric sensors and also in RRAM [10]. However, once at the sub-micron scale, polycrystalline materials usually perform worse than single-crystalline ones. The piezoelectric response of polycrystalline compounds is reduced due to the averaging effect of the piezoelectric constants along the different crystallographic directions and the occurrence of domain-wall displacements in ferroelectric piezoelectrics [11]. In the case of resistive switching, the presence of grain boundaries induces variations in the conductive filaments paths upon successive cycling [12], leading to a scattering in the on/off voltage values [10]. From all the aforementioned, it is expected that synergistic effects can be achieved in *nanostructures* that are *porous* and *single-crystalline* at the same time. However, although much effort has been made to produce, separately, porous [13-15] and single-crystal nanomaterials [16-18], synthesizing porous single-crystalline nanostructures is not straightforward and it often requires of multi-step sophisticated procedures [19-21].

To fulfil certain technological demands, multifunctional materials (either single-phase or hybrid composites) are needed. Among metals and semiconductors, ZnO is one of the materials that satisfies the definition of "multifunctional" and has been employed in diverse fields, including electrochemistry, electromechanics, photocatalysis and electronic applications, among others [22,23]. The multifunctionality of ZnO stems from the unique features of its thermodynamically stable crystallographic phase, the wurzite structure, which belongs to the non-centrosymmetric $P6_3mc$ space group. In this crystallographic structure, both Zn and O atoms are tetrahedrally coordinated to each other, forming two compact hexagonal sublattices one for each kind of atom [24]. This layered structure leads to two polar surfaces, which is the key point in several physical properties of ZnO, such as luminescence or piezoelectricity.

In this work, we present a self-templating and cost-effective hydrothermal procedure that enables the production of large areas of either faceted or spongy single-crystalline ZnO nanorods (NRds) from previously electrodeposited Zn films. Hydrothermal treatments had been previously used to synthesize ZnO nanotubes for photocatalytic applications [25] and nanorods and NRds with photoluminescence properties [26]. Herein, the morphology of the NRds can be adjusted (faceted *versus* spongy), without losing the single-crystalline character, by varying the electrodeposition parameters of the parent Zn film. The obtained NRds exhibit piezoelectric properties and resistive switching behaviour, which depend on the intrinsic morphology of the single-crystalline NRds.

2. Materials and Methods

2.1. Synthesis of Faceted and Spongy Single-Crystal ZnO Nanorods

All the chemical reagents were of analytical grade and were used as received: zinc sulphate heptahydrate ($ZnSO_4 \cdot 7H_2O$ puriss 99.0%), sodium sulphate anhydrous (Na_2SO_4, ACS reagent ≥99.0%), boric acid (H_3BO_3, puriss p.a. ACS reagent ≥99.8%) and sulfuric acid (H_2SO_4, reagent grade, 95-98%).

The synthetic approach to obtain the faceted and spongy single crystal ZnO NRds combines two different techniques: electrodeposition and hydrothermal treatments. First, two types of Zn films were grown by electrodeposition. This is a very versatile and cost-effective technique since it requires neither vacuum conditions nor the use of clean room facilities. Zn electrodeposition was carried out in a one-compartment thermostatized three-electrode cell using a PGSTAT302N Autolab potentiostat/galvanostat (Ecochemie). Si substrates with Ti and Au evaporated layers were used as working electrodes (WE), which were positioned vertically within the electrolyte. The working area was set to 0.25 cm^2. A double junction Ag|AgCl (E = +0.210 V versus standard hydrogen electrode (SHE)) reference electrode (Metrohm AG) was used with 3 M potassium chloride (KCl) inner solution and an interchangeable outer solution. The outer solution was made of 1 M sodium sulphate. A platinum spiral served as the counter electrode. The temperature was fixed to 25°C. Prior to each deposition, the bath was deaerated by gently bubbling N_2 during 15 min. The Zn film used as a precursor for the growth of faceted single crystal ZnO NRds (F_Zn Film) was deposited galvanostatically at a current density (j) of -10 mA cm^{-2} during 1800 s in an electrolyte consisting of 0.1 M $ZnSO_4 \cdot 7H_2O$, 0.1 M Na_2SO_4 and 0.1 M H_3BO_3. The Zn film employed for the growth of the spongy single crystal ZnO NRds (SP_Zn Film) was deposited potentiostatically at a potential (E) of -1.5 V in an electrolyte composed of 0.1 M $ZnSO_4 \cdot 7H_2O$ during 400 s. Ultrapure water (18 MΩ cm) was used to prepare the plating solutions and the pH was adjusted to pH = 2 with H_2SO_4 in both cases. In a

second step, the plated Zn films were introduced in a distilled water bath, at 90 ºC, for 8 h. During this hydrothermal treatment, the ZnO growth took place. After the treatment, the samples were removed from the bath and dried in air to stop the NRds from further growth.

2.2.Structural and morphological characterization of the Zn films and ZnO nanorods

The crystallographic phases present in each sample were determined by X-ray diffraction (XRD) in a Philips X'Pert diffractometer using the Cu K_α radiation (40 kV and 30 mA), a step size of 0.026º and an integration time of 400 s in the 30°–65° 2θ range. The crystallographic structure was also analyzed by high resolution transmission electron microscopy (HRTEM) and selected area electron diffraction (SAED) utilizing a JEOL-JEM 2011 system operated at 200 kV. The morphology and energy dispersive x-ray mappings (EDX) of the NRds was examined by field emission scanning electron microscopy (FE-SEM) using a Zeiss MERLIN microscope operated at 3.0 kV and 100 pA to prevent from charging effects. EDX mappings were obtained at 20kV and 1nA.

2.3.Assessment of the piezoelectric and resistive switching properties of the ZnO nanorods

The piezoelectric properties were studied by piezoresponse force microscopy (PFM) with a Keysight 5500LS AFM using a solid platinum conductive tip with reference RMN-25PT300B from Rockymotauntain Nanotechnology. This is a special probe that consists of a long tip attached to a cantilever with a spring constant of 18 N m^{-1}. Such setup effectively minimizes artifacts and electrostatic phenomena that can interfere with measurements, giving too high or false D33 constants [27,28]. All the measurements were carried out in low humidity conditions (less than 5%) to avoid possible

electrochemical artifacts. A total of 40 sweeps in different points along the sample were acquired for statistical purposes. The sweeps that provided no piezoelectric signal were not considered, as they were assumed to have been performed onto the metallic Zn substrate (arising from sample defects) or from non-piezoelectric facets of the ZnO nanorods [29]. The tip calibration was performed through the measurement of the deflection *versus* distance curve [30].

Transport properties were examined with the same AFM, including a current-to-voltage amplifier "Resiscope" capable of measuring 10 decades of current. The charge transport study was performed acquiring current *versus* voltage curves, sweeping bias from -4 V to +5 V and back to -4 V. The specific voltages used were selected as they were high enough to change the conductivity state of the sample but not exceedingly high so as to destroy the tip, cause undesirable electrochemistry effects or deteriorate the sample. The sweep rate was kept constant to 15 V s^{-1}, while low humidity (less than 5%) was again maintained for all the measurements. The force used, for both PFM and conductive atomic force microscopy (CAFM), was in the range of 1-10 μN.

3. Results and discussion

The XRD patterns (**Figure 1**) reveal that both Zn films possess the hexagonal-close packed (hcp) structure (space group *P63/mmc*), with preferential orientation along the [002] direction. In the diffractograms from the hot-water treated samples, clear peaks from the ZnO wurtzite phase, arising from the formation of the NRds, are visible, superimposed to peaks from Zn. Semi-quantitative information about texture can be obtained from the relative intensity of the XRD peaks, i.e., normalizing the patterns by the most intense XRD peak (discarding those related to the substrate) and comparing them with the values corresponding to crystallographically isotropic Zn and ZnO.

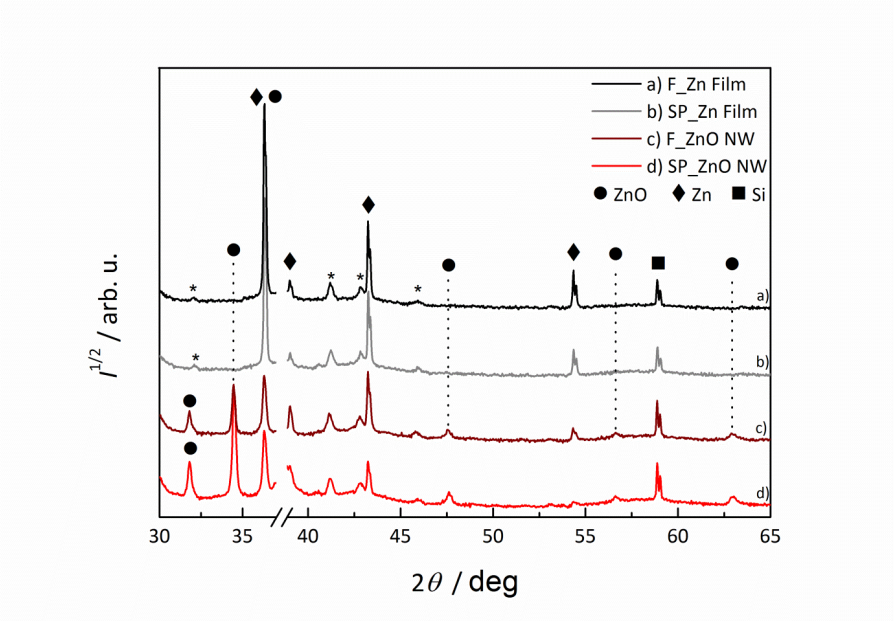

Figure 1. XRD patterns for the electrodeposited F_Zn, SP_Zn films and the F_ZnO and SP_ZnO NRd samples. The Zn peaks can be indexed according to the JCPDS 04-0831 and the ZnO peaks according to the JCPDS 36-1451. The cut around $2\theta = 38°$ is to hide the high intensity Au (111) peak (JCPDS 04-0784) from the substrate. * belongs to intermetallic $AuZn_3$.

Table 1 lists the five most intense reflections for the four investigated samples, together with the relative peak intensity obtained experimentally and, in parenthesis, theoretically values for isotropic powders, as tabulated in the JCPDS cards. The results reveal that Zn films tend to grow in the basal plane [002] direction, which presents the highest experimental relative intensity. Peaks like the (100) or (101) show a significant loss in intensity compared to the tabulated values. For the F-ZnO and SP_ZnO NRds the analysis is more subtle due to the mixed contribution between Zn and ZnO in the 2θ peak at 36.3º. However, one remarkable aspect is the notorious increment in the (002) peak intensity in both types of NRds. This can be understood as a consequence of the tendency for the NRds to preferential grow along the [002] direction (*c*-axis) and remain aligned perpendicular to the substrate. The additional peaks in Figure 1, marked with an

asterisk, correspond to intermetallic $AuZn_3$ phase, which presumably forms during the initial stages of the Zn electroplating, due to the diffusion of Zn into the Au [31].

Peak (º) (plane)	**Intensity**	**Peak (º) (plane)**	**Intensity**	**Peak (º) (plane)**	**Intensity**	**Peak (º) (plane)**	**Intensity**
F_Zn Film		**SP_Zn Film**		**F_ZnO NRds**		**SP_ZnO NRds**	
36.331 (002)	100% (53.00%)	36.329 (002)	100% (53.00%)	31.807 (100)	28.83% (57.00%)	31.806 (100)	44.23% (57.00%)
39.008 (100)	14.71% (40.00%)	39.039 (100)	13.47% (40.00%)	34.422 (002)	77.86% (44.00%)	34.484 (002)	100% (44.00%)
43.247 (101)	43.30% (100%)	43.273 (101)	47.89% (100%)	36.253* *(101)*	*100% (100%)*	36.307* *(101)*	*69.07% (100%)*
54.348 (102)	19.52% (28.00%)	54.347 (102)	15.35% (28.00%)	47.539 (102)	8.54% (23%)	47.611 (102)	20.34% (23%)
70.075 (103)	20.12% (25.00%)	70.106 (103)	11.96% (25.00%)	56.603 (110)	6.46% (32%)	56.595 (110)	17.01% (32%)

Table 1. List of XRD peaks positions, together with the experimental and tabulated (in parenthesis) relative intensity. Indicated in the first four left columns are the peaks positions and the corresponding crystallographic planes for Zn (JCPDS 04-0831) for the F_Zn and SP_Zn Films. Indicated in the four right columns are the peaks positions and the related plane for the ZnO (JCPDS 36-1451) for both faceted (F-ZnO) and spongy (SP-ZnO) NRds. The values marked with * correspond to peaks whose positions coincide for both Zn and ZnO.

The Zn films and ZnO NRds were morphologically investigated by field-emission scanning electron microscopy (FE-SEM). Zn films consist of hexagonal crystals stacked to each other parallel or almost parallel to the substrate (**Figure 2a and 2c**). Notice that although both films are structurally equivalent, their grain morphology is actually different. The grains in the F-Zn film exhibit a more faceted or stratified architecture than those in SP-Zn film. The NRds probably inherit the morphology of the parent Zn film to

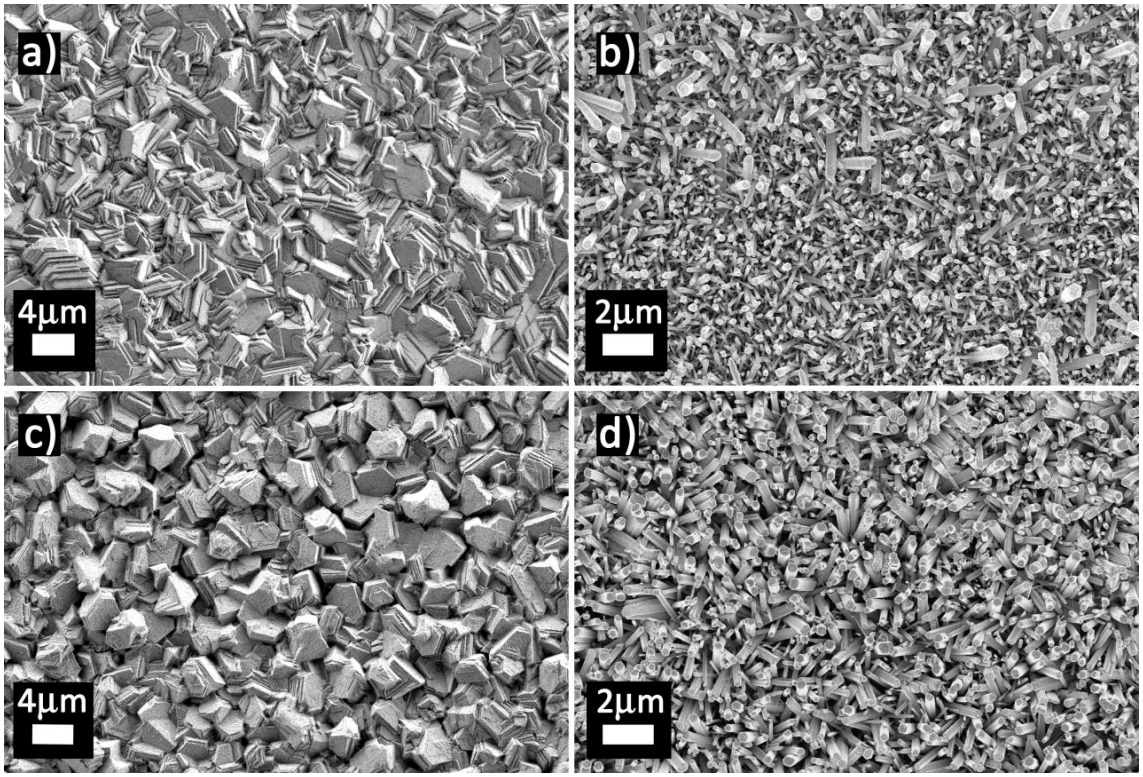

Figure 2. SEM images corresponding to: a) F-Zn, b) F-ZnO, c) SP-Zn and d) SP-ZnO samples.

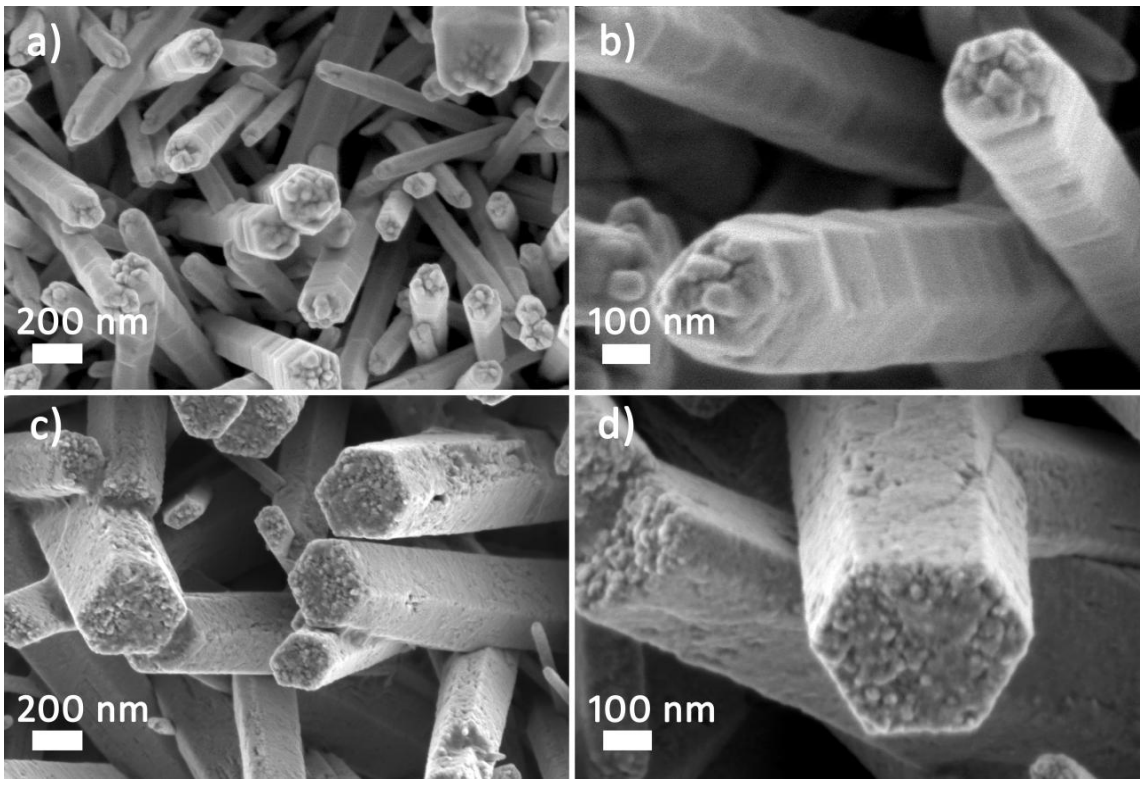

Figure 3. Field emission SEM images of a, b) faceted and c, d) spongy ZnO NRds.

some extent. In turn, the low magnification SEM images of the ZnO NRds (**Figure 2b and 2d**) confirm the tendency of the NRds to grow along the *c*-axis orientation during the hot water treatment. Due to the difficulty to disentangle the ZnO (101) contribution from de Zn (002) in the XRD pattern, which may give us an idea of how deviated from an ideal perpendicular array are our nanorods [32], SEM cross section have been obtained. **Figure S1** confirms, apart from the c-axis growth tendency of the NRds, that most of the nanorods are deviated by an angle smaller than 30º. The tilt has been calculated measuring 100 NRds resulting, on average, that faceted nanorods are deviated by an angle of (16.0±11.9) degrees and by (15.6±11.3) degrees the spongy NRds. Further details of the angular distribution are shown in **Figure S2**.

EDX mappings (**Figure S3**) showed the element distribution (Zn and O) for both types of samples. While Zn showed a uniform distribution, O presents some dark regions. These black regions can be ascribed to a shadowing effect due to sample roughness, but also to a lack of ZnO NRds coverage. In order to disentangle both plausible origins, the coverage of the NRds has been determined segmenting the SEM images (**Figure S4**) applying a binary threshold. In both cases the coverage is higher than 90%, suggesting that dark regions are originated by shadowing effects (see **Table S1**). High magnification images of the ZnO NRds are shown in **Figure 3**. The images reveal the distinct morphology (faceted *versus* spongy) of the NRds prepared from the F-Zn and SP-Zn films. Some regions of the spongy NRds seem to exhibit nanoporosity with pore size that lies below 10 nm. In both cases, though, the NRds exhibit a hexagonal cross section, suggesting that they are single-crystalline. **Table 2** summarizes the average sizes (length and width) for both faceted and spongy, determined counting 30 NRds (see supporting information for histograms (**Figure S5**)).

	Length (µm)	Width (µm)
Faceted	(1.81±0.88)	(0.20±0.12)
Spongy	(1.48±0.66)	(0.24±0.09)

Table 2. Average sizes for both faceted and spongy nanorods.

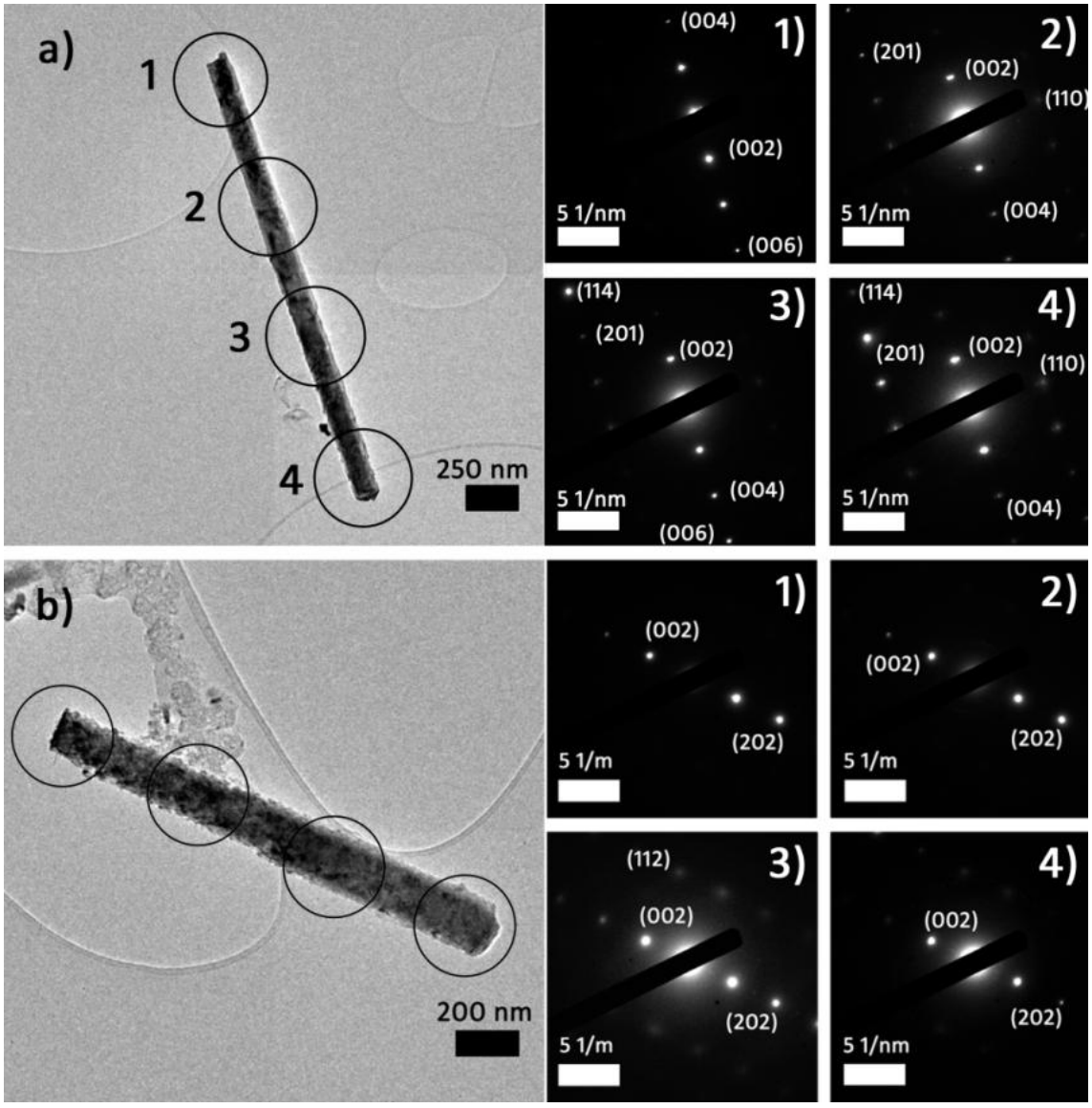

Figure 4. TEM images of a single a) faceted and b) spongy ZnO NRd. The insets in a) and b) correspond to high-resolution TEM images. The 1) to 4) panels next to a) and b) are the corresponding SAED patterns measured along the NRd axis, as indicated in the figure.

The crystal structure was also evaluated by high resolution transmission electron microscopy (HRTEM) and selected area electron diffraction (SAED) (**Figure 4**). HRTEM images (**Figure S6 a) and b)**) reveal a crystalline structure with an interplanar distance of ~2.58 Å, corresponding to the (002) planes, which are oriented perpendicular to the growth direction of the NRds. Selected area electron diffraction (SAED) patterns confirmed the single-crystal nature of the NRds. Namely, SAED analyses performed along the *c*-axis of the two types of NRds revealed spotty patterns in both cases, which did not vary along the length of the NRds. From Figure 4b can be easily seen that small nanoparticles coat the spongy nanorod. HR-TEM image (**Figure S7**) of these nanoparticles provided some structural insights. Figure S7 shows up that the nanoparticles are crystalline, formed by planes with an interplanar distance of 2.79A corresponding to the ZnO (100) plane. These planes are stacked with a certain angle with respect to the nanorod growth direction (002). This deviation suggest that its formation is posterior to the nanorod growth, acting the nanorod's surface as a nucleation point. In any case, we believe that, since these nanoparticles at the nanorods' surface are very small compared to the dimensions of the nanorods, the main contribution to the measured piezoelectric and resistive switching properties arises from their virtually single-crystalline character.

The piezoelectric properties of both faceted and spongy NRds were investigated through the use of piezoresponse force microscopy (PFM) [27,28,33,34]. A conductive tip was put in contact with the sample surface while an AC bias was applied. The AC bias induces the material to expand and contract at the same AC frequency as the applied bias. Several acquisitions of the Tip amplitude vibration *versus* Applied AC voltage were performed (see **Figure 5a**). The tip vibration amplitude showed a linear

dependence on the applied AC bias amplitude, as expected from a piezoelectric signal [35]. More importantly, special selected tips were employed in order to reduce possible electrostatic effects that may affect the electromechanical behavior of the NRds, in order to provide a clean and trustful electromechanical response [36]. Further Force-vs-Displacement curves were obtained to calibrate the system while the resonance peak maximum values were studied for different applied bias amplitude (**see Figure S8**).

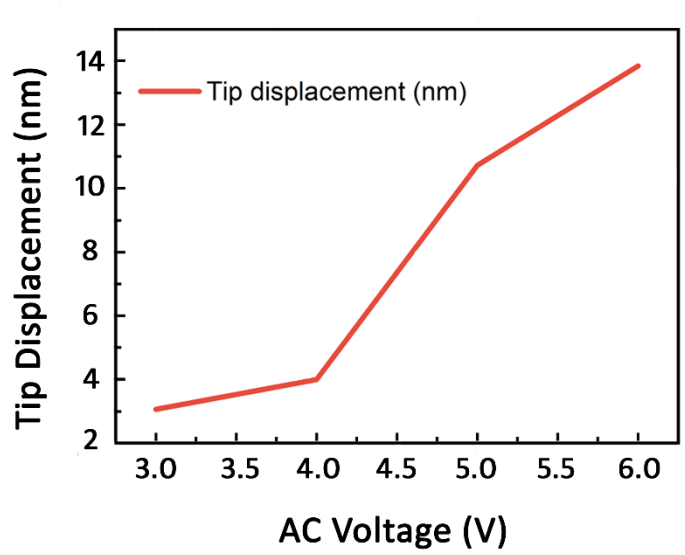

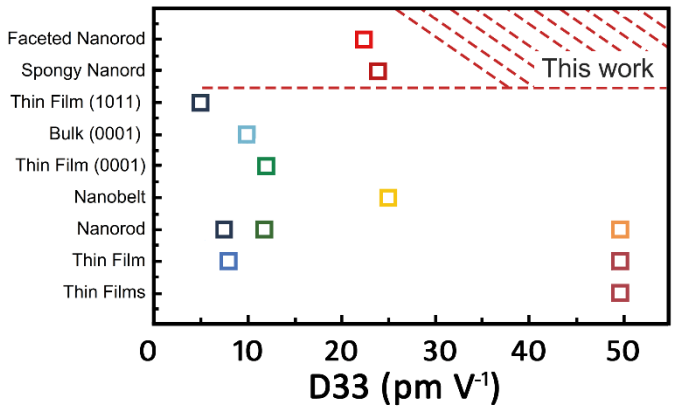

Figure 5: a) Tip displacement vs AC Voltage plot and b) scheme comparing the D33 results of this work results with the literature.

The D33 piezoelectric coefficient was obtained analyzing the resonance curves [37] for both the F-ZnO and SP_ZnO NRds. The statistical analysis for each sample result in a D33 values of 22.4 ± 3.2 pm V^{-1} and 23.9 ± 2.7 pm V^{-1}, respectively.

Remarkably, the obtained values of D33 are larger than the expected piezoelectric coefficient for bulk ZnO (D33 = 9.93 pm V^{-1}). **Figure 5b** summarizes the D33 values for different ZnO nanostructures, textured thin films and bulk samples [30, 32, 38-42]. Our results fall within the upper range values previously measured. One of the possible reasons why the D33 of our nanorods are higher than the bulk, a part from its single-crystalline nature, is recently reported by Kang et al. who demonstrated that the reduced lateral size of the nanorods improve the piezoresponse by relaxing the clamping effect [43]. These results also reveal that nanoporosity in SP-ZnO NRds is not detrimental for the piezoelectric properties. Moreover, since SP-ZnO NRds have a larger diameter than F-ZnO, one might expect a lower D33 value for SP-ZnO NRds, but this is actually not experimentally observed. In addition, note that the misalignment among the NRds (with respect to the vertical direction) might eventually result in an underestimation of D33. In other words, when a bias is applied to a NRd canted by an amount ϕ, it will expand in its c-axis (nanorod longitudinal axis), however, the resulting tip displacement will be reduced by a factor cosine of ϕ (orthogonal projection with respect to the substrate). Putting some numbers, for a maximum tilt of 30º (in the edge of the determined angular distribution), the underestimation assumed is smaller than the 15%. Also note that the other piezoelectric constants in ZnO (D31 and D15) are actually negative [44].

Moreover, the tilt present in the nanorods may introduce a new hindrance by limiting the expansion each other. Despite these limitations, the good piezoelectric behaviour shown by the nanorods, make them appealing to be use in strain-dependent nanosensors or nanoactuators [45,46].

Charge transport properties were investigated through the use of a conductive atomic force microscopy (CAFM). The setup is depicted in **Figure 6a**, where it is shown that the sample is biased with a given voltage, while the tip is grounded.

The obtained charge transport results are shown for the F-ZnO and SP-ZnO NRds in **Figure 6c** and **6d**, respectively. The sweep starts at -4 V, where a low resistance state (LRS) is recorded. Bias is increased from -4 V to +5 V (dark blue symbols) and a high resistance state (HRS) is recorded at +5 V. The sweep is then reversed, from +5 V to -4 V (orange symbols), where the LRS is recovered. Comparing the results from F-ZnO and SP-ZnO NRds one can see that both samples render a similar level of current. This behavior confirms the nature of charge transport, as being essentially an interface effect because for a volume effect, one should expect lower currents when the porosity of the NRds increases, as the effective cross section is then diminished and also discards any possible contribution due to nanorod intercontection. The specific SET and RESET voltages are slightly different for both types of NRds. The exact values for these voltages depend upon many factors, like vacancy concentration and interface quality that could shift the SBH and hence the threshold voltages. Upon performing the sweeps, we also found metallic-like charge transport behavior that can be correlated, as in PFM, with the existence of the metallic substrate due to defects produced during the sample manipulation.

Looking from the bottom, the structure is composed of a metal (Zinc), a semiconductor (ZnO) and another metal (Platinum, which is the CAFM tip) acting as a top electrode. A metal-semiconductor-metal (M-S-M) structure is hence formed [47]. The specific charge transport nature of the structure is under debate [48,49], however the ionic mobility inside the semiconductor seems to be the dominant effect [47]. The M-S-M structure can be modeled as two Schottky Barrier Heights (SBH), one located in each end of the NRd (see **Figure 6b**) [50]. The two SBH are modulated through different ionic diffusion present in the semiconductor, that will increase or decrease the specific barrier height at each interface. Throughout the structure, charge transport is thus modulated by an interface effect, the metal/semiconductor interface. The specific type of ions diffused are generally oxygen vacancies, but other type of ionic movement has been reported to also cause a change in the SBH [51]. For oxygen vacancies, their presence near the interface will effectively reduce the SBH. On the contrary, a reduction of oxygen vacancies near the interface will increase the SBH [47,52].

However, the step-like response of the yellow line in figure 5d may induce the reader to think into a filamentary RS mechanism, as previously investigated by other authors showing possible filamentary mechanism for similar structures like Cu-ZnO-Pt junctions as well as filamentary formation along the nanorods [53,54]. Moreover, elucidate the real mechanism of the resistive switching phenomena is out of the scope of this paper.

The retention time for both the LRS and HRS was measured in both samples, to ensure both states could be read (data shown in **Figure 6e** and **6f**). In order to perform this experiment, a LRS was recorded with -4 V during 10 seconds. Afterwards, the sample was biased with -2 V, and the LRS evolution with time was recorded (black line). A step voltage of +5 V was then set to record the HRS while, after 10 seconds, a -2 V bias

was placed again to record the HRS evolution with time (red line). The observation of resistive switching properties in these NRds is in agreement with previous works on ZnO nanorods [55] and could be of interest for nanoscale non-volatile resistive memory devices for sensor applications. In combination with the piezoelectric response, such types of nanostructured objects could also be used for programmable electromechanical memories [56].

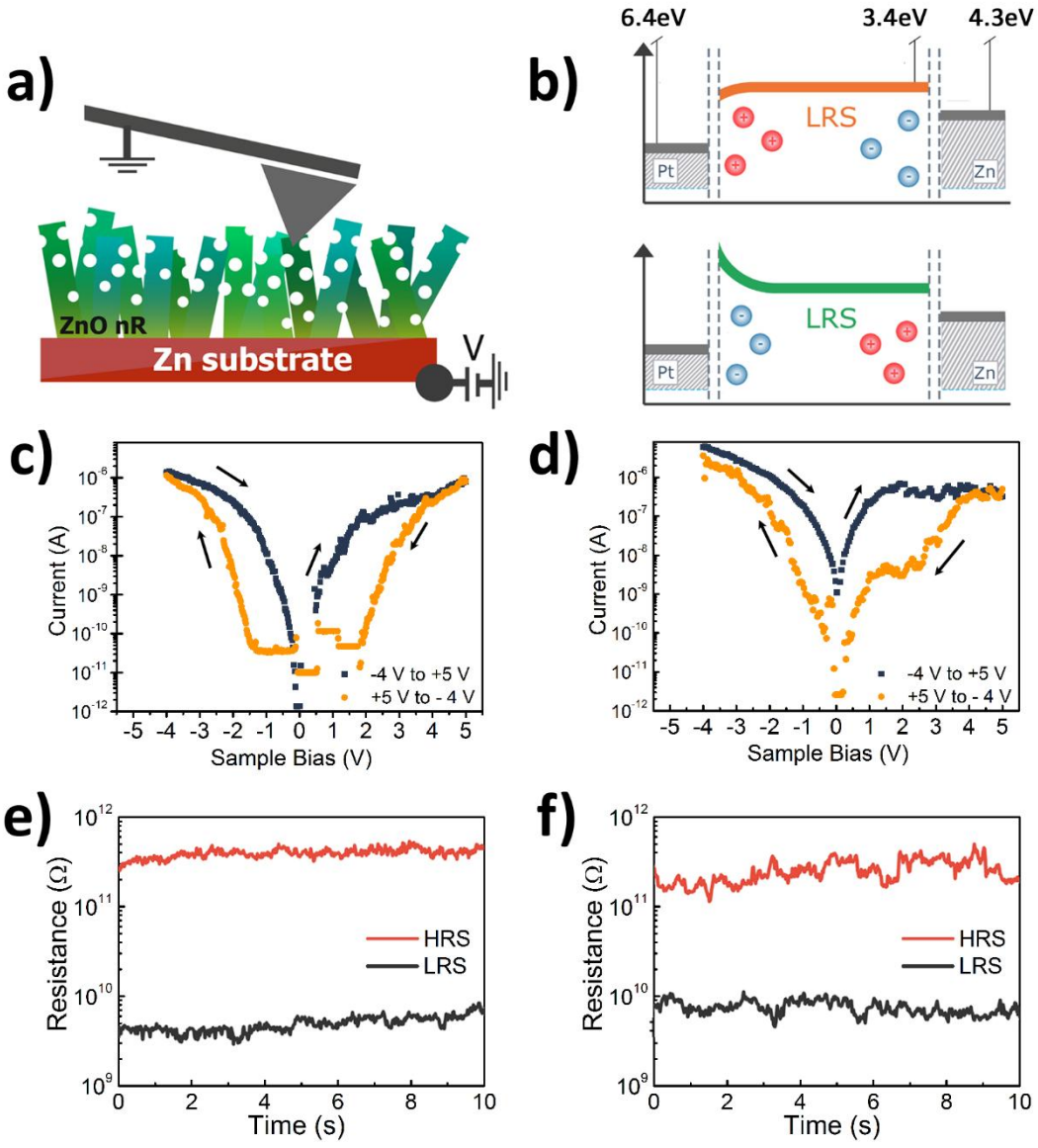

Figure 6. a) Schematic diagram for Current Atomic Force Microscopy (CAFM) measurements. The sample is biased with a given voltage while the current flows through the sample to the grounded tip. b) Energy band diagram of the Metal-Semiconductor-Metal structure. c, d) Current versus Voltage spectroscopy curves

obtained for faceted and spongy ZnO NRds, respectively. e, f) Resistance versus time evolution of a low resistance state (LRS) –black line–, and a high resistance state (HRS) –red line– for the faceted and spongy NRds, respectively.

Conclusions

In summary, a versatile hydrothermal method to prepare large arrays of single-crystalline ZnO NRds with tunable morphology has been presented. The morphology of the ZnO NRds seems to be dependent on the electrodeposited parent Zn Film. The obtained NRds show a piezoelectric response larger than for bulk ZnO and higher to other reported ZnO Nanorods. Its small lateral size and single crystallinity are plausible motive to this large piezoresponse. It is also demonstrated that piezoelectric properties are independent on the surface porosity. The resistive switching behaviour of both faceted and spongy is also reported and, as in the case of the piezoelectric, minor differences are seen in porous single-crystal nanorods. By all these above reasons the presented nanorods open a paradigm for sensor and actuator applications where synergic effects are required (large area materials and electromechanic properties).

Acknowledgements

Financial support by the Spanish Government [Project MAT2014-57960-C3-1-R and associated FEDER], the Generalitat de Catalunya (2014-SGR-1015) and the European Research Council (SPIN-PORICS 2014-Consolidator Grant, Agreement nº 648454) is

acknowledged. E.P. is grateful to MINECO for the “Ramon y Cajal” contract (RYC-2012-10839)

Supporting Information

Additional data related to structural and piezoelectric measurements can be found in supporting information (Figures S1 to S8).

Corresponding Author

*Alberto Quintana: alberto.quintana@uab.cat

* Andrés Gómez: agomez@icmab.es

* Prof. Jordi Sort: jordi.sort@uab.cat

References

1. X. Tong, X. Xia, C. Guo, Y. Zhang, J. Tu, H. J. Fan, X.-Y. Guo, Efficient Oxygen Reduction Reaction Using Mesoporous Ni-doped Co_3O_4 Nanowire Array Electrocatalysts. Mater. Chem. A, 2015, 3, 18372-18379.

2. G. Wang, Y. Yang, J.-H. Lee, V. Abramova, H. Fei, G. Ruan, E. L. Thomas, J. M. Tour, Nanoporous Silicon Oxide Memory. Nano Lett. 2014, 14, 4694-4699.

3. Y. Fan, S. W. King, J. Bielefeld, M. K. Orlowski, Characterization of Porous BEOL Dielectrics for Resistive Switching. ECS Trans. 2016, 72, 35-50.

4. H Gullapalli, V. S. M. Vemuru, A. Kumar, A. Botello-Mendez, R. Vajtai, M. Terrones, S. Nagarajaiah, P. M. Ajayan, Flexible Piezoelectric ZnO–Paper Nanocomposite Strain Sensor. Small 2010, 6, 1641-1646.

5. A. Castro, P. Ferreira, B. J. Rodriguez, P. M. Vilarinho, The Role of Nanoporosity on the Local Piezo and Ferroelectric Properties of Lead Titanate Thin Films. J. Mater. Chem. C 2015, 3, 1035-1043.

6. R. Agrawal, H. D. Espinosa, Giant Piezoelectric Size Effects in Zinc Oxide and Gallium Nitride Nanowires. A First Principles Investigation. Nano lett. 2011, 11, 786-790.

7. A. Menzel, K. Subannajui, F. Güder, D. Moser, O. Paul, M. Zacharias, Multifunctional ZnO-Nanowire-Based Sensor. Adv. Funct. Mater. 2011, 21, 4342-4348.

8. S. Iijima, Helical Microtubules of Graphitic Carbon. Nature 1991, 354, 56-58.

9. Z. L. Wang, Nanostructures of Zinc Oxide. Mater. Today 2004, 7, 26-33.

10. W.-Y. Chang, C.-A. Lin, J.-H. He, T.-B. Wu, Resistive Switching Behaviors of ZnO Nanorod Layers Appl. Phys. Lett. 2010, 96, 242109.

11. D. Damjanovic, Ferroelectric, Dielectric and Piezoelectric Properties of Ferroelectric Thin Films and Ceramics. Rep. Prog. Phys. 1998, 61, 1267-1324.

12. Y. Yang, X. Zhang, M. Gao, F. Zeng, W. Zhou, S. Xie, F. Pan, Nonvolatile Resistive Switching in Single Crystalline ZnO Nanowires. Nanoscale 2011, 3, 1917-1921.

13. F.-X. Ma, H. B. Wu, C.-Y. Xu, L. Zhen, X. W. Lou, Self-Organized Sheaf-Like Fe3O4/C Hierarchical Microrods with Superior Lithium Storage Properties. Nanoscale 2015, 7, 4411-4414.

14. B. Zhou, S. Yang, L. Wu, W. Wu, W. Wei, L. Chen, H. Zhang, J. Pan, X. Xiong, Amorphous Carbon Framework Stabilized SnO_2 Porous Nanowires As High Performance Li-ion Battery Anode Materials. RSC Adv. 2015, 5, 49926-49932.

15. G. Ma, X. Wang, Synthesis and Applications of One-Dimensional Porous Nanowire Arrays: A Review. Nano 2015, 10, 1530001.

16. J. Goldberger, R. He, Y. Zhang, S. Lee, S. H. Yan, H.-J. Choi, P. Yang, Single-Crystal Gallium Nitride Nanotubes. Nature 2003, 422, 599-602.

17. H. Zhu, J. Deng, J. Chem, R. Yu, X. Xing, Growth of Hematite Nanowire Arrays During Dense Pentlandite Oxidation. J. Mater. Chem. A 2014, 2, 3008-3014.

18. Z. R. Tian, J. A. Voigt, J. Liu, B. McKenzie, M. J. McDermott, M. A. Rodriguez, H. Konishi, H. Xu, Complex and Oriented ZnO Nanostructures. Nat. Mater. 2003, 2, 821-826.

19. X. W. Lou, D. Deng, J. Y. Lee, L. A. Archer, Thermal formation of mesoporous single-crystal Co_3O_4 nano-needles and their lithium storage properties. J. Mater. Chem., 2008, 18, 4397–4401.

20. M. Liu, S He, W. Chen, Co_3O_4 Nnanowires Supported on 3D N-doped Carbon Foam as an Electrochemical Sensing Platform for Efficient H_2O_2 detection. Nanoscale 2014, 6, 11769-11776.

21. X. Wang, C. J. Summers, Z. L. Wang, Mesoporous Single-Crystal ZnO Nanowires Epitaxially Sheathed with Zn_2SiO_4. Adv. Mater. 2004, 16, 1215-1218.

22. Z. L. Wang, J. Song, Piezoelectric Nanogenerators Based on Zinc Oxide Nanowire Arrays. Science 2006, 312, 242-246.

23. H. Kind, H. Yan, B. Messer, M. Law, P. Yang, Nanowire Ultraviolet Photodetectors and Optical Switches. Adv. Mater. 2002, 14, 158-160.

24. C. Klingshrin, ZnO: Material, Physics and Applications. ChemPhysChem 2007, 8, 782-803.

25. H. Wang, G. Li, L. Jia, G. Wang, C. Tang, Controllable Preferential-Etching Synthesis and Photocatalytic Activity of Porous ZnO Nanotubes. J. Phys. Chem. C 2008, 112, 11738-11743.

26. W. K. Tan, K. A. Razak, Z. Lockman, G. Kawamura, H. Muto, A. Matsuda, Formation of Highly Crystallized ZnO Nanostructures by Hot-Water Treatment of Etched Zn Foils. Mater. Lett. 2013, 91, 111-114.

27. N. Balke, P. Maksymovych, S. Jesse, A. Herklotz, A. Tselev, C.-B. Eom, I. I. Kravchenko, P. Yu, S. V. Kalinin, Differentiating Ferroelectric and Nonferroelectric Electromechanical Effects with Scanning Probe Microscopy. ACS Nano 2015, 9, 6484-6492.

28. M. Andrä, F. Gunkel, C. Bäumer, C. Xu, R. Dittmann, R. Waser, The Influence of the Local Oxygen Vacancy Concentration on the Piezoresponse of Strontium Titanate Thin Films Nanoscale 2015, 7, 14351-14357.

29. C. Harnagea, A. Pignolet, M. Alexe, D. Hesse, Piezoresponse Scanning Force Microscopy: What Quantitative Information Can We Really Get Out of Piezoresponse Measurements on Ferroelectric Thin Films. Integr. Ferroelectr. 2002, 44, 113-124.

30. M.-H. Zhao , Z.-L. Wang,S. X. Mao, Piezoelectric Characterization of Individual Zinc Oxide Nanobelt Probed by Piezoresponse Force Microscope. Nano Lett. 2004, 4 587–590

31. D. Borissov, A. Pareek, F. U. Renner, M. Rohwerder, Electrodeposition of Zn and Au–Zn Alloys at Low Temperature in an Ionic Liquid. Phys. Chem. Chem. Phys. 2010, 12, 2059-2062.

32. D. Tamvakos, S. Lepadatu, V.-A. Antohe, A. Tamvakos, P. M. Weaver, L. Piraux, M. G. Cain, D. Pullini, Piezoelectric properties of template-free electrochemically grown ZnO nanorod arrays. Appl. Surf. Sci. 2015, 356 1214-1220.

33. A. L. Kholkin, S. V. Kalinin, A. Roelofs, A. Gruverman, In Scanning Probe Microscopy. Electrical and Electromechanical Phenomena at the Nanoscale, S. V. Kalinin, A. Gruverman, Eds.; Springer, New York, 2007, Chapter 6, pp 173-214.

34. S. V. Kalinin, A. Rar, S. A. Jesse, Decade of Piezoresponse Force Microscopy: Progress, Challenges, and Opportunities. IEEE Trans. Ultrason. Ferroelectr. Freq. Control 2006, 53, 2226-2252.

35. D. A. Bonnell, S. V. Kalinin, A. L. Kholkin, A. Gruverman, Piezoresponse Force Microscopy: A Window into Electromechanical Behavior at the Nanoscale. MRS Bull. 2009, 34, 648-657.

36. arXiv:1610.01809

37. J. L. Hutter, J. Bechhoefer, Calibration of atomic-force microscope tips. Rev. Sci. Instrum. 1993, 64, 1868-1873.

38. I. K. Bdikin, J. Gracio, R. Ayouchi, R. Schwarz and A. L. Kholkin, Local piezoelectric properties of ZnO thin films prepared by RF-plasma-assisted pulsed-laser deposition method. Nanotechnology 2010, 21 235703.

39. M. Laurenti, S. Stassi, M. Lorenzoni, M. Fontana, G. Canavese, V. Cauda,C. F. Pirri, Evaluation of the piezoelectric properties and voltage generation of flexible zinc oxide thin films. Nanotechnology 2015, 26 215704.

40. H. J. Fan, W. Lee, R. Hauschild, M. Alexe, G. Le Rhun, R. Scholz, A. Dadgar, K. Nielsch, H. Kalt, A. Krost, M. Zacharias, U. Gösele, Template-Assisted Large-Scale Ordered Arrays of ZnO Pillars for Optical and Piezoelectric Applications. Small 2006, 4 1214-1220.

41. M. Ghosh, S. Ghosh, M. Seibt, K. Y. Rao, P. Peretzkic, G. M. Rao, Ferroelectric origin in one-dimensional undoped ZnO towards high electromechanical response. CrystEngComm, 2016, 18 622-630.

42. W. Qin, T. Li, Y. Li, J. Qiu, X. Ma, X. Chen, X. Hu, W. Zhang, A high power ZnO thin film piezoelectric generator. Appl. Surf. Sci. 2016, 364, 670-675.

43. M. Gyu. Kang, S.-Y. Lee, D. Maurya, C. Winkler, H.-C. Song, R. B. Moore, M. Sanghadasa, S. Priya, Wafer-Scale Single-Crystalline Ferroelectric Perovskite Nanorod Arrays. Adv. Funct. Mater. 2017,x,1701542.

44. T. Hanada, In Oxide and nitride semiconductors: Processing, properties and applications, T. Yao, S.-K. Hong, Eds.; Springer-Verlag, Berlin Heidelberg, 2009, Chapter 1, pp 1-19.

45. Z. Wang, J. Zhou, J. Song, J. Liu, N. Xu, Z. L. Wang, Piezoelectric Field Effect Transistor and Nanoforce Sensor Based on a Single ZnO Nanowire. Nano Lett. 2006, 6, 2768-2772.

46. P. Wang, Y. Fu, B. Yu, Y. Zhao, L. Xing, X. Xue, Realizing room-temperature self-powered ethanol sensing of ZnO nanowire arrays by combining their piezoelectric, photoelectric and gas sensing characteristics. J. Mater. Chem. A, 2015, 3, 3529-3535.

47. J. J. Yang, M. D. Pickett, X. Li, D. A. A. Ohlberg, D. R. Stewart, R. S. Williams, Memristive Switching Mechanism for Metal/Oxide/Metal Nanodevices. Nature Nanotech. 2008, 3, 429-433.

48. R. Waser, M. Aono, Nanoionics-Based Resistive Switching Memories. Nature Mater. 2007, 6, 833-840.

49. B. J. Choi, D. S. Jeong, S. K. Kim, C. Rohde, S. Choi, J. H. Oh, H. J. Kim, C. S. Hwang, K. Szot, R. Waser, R. Reichenberg, S. Tiedke, Resistive Switching Mechanism of TiO_2 Thin Films Grown by Atomic-Layer Deposition. J. Appl. Phys. 2005, 98, 033715.

50. Z. L. Wang, ZnO Nanowire and Nanobelt Platform for Nanotechnology. Mater. Sci. Eng., R 2009, 64, 33–71.

51. L. Schmidt-Mende, J. L. MacManus-Driscoll, ZnO – Nanostructures, Defects, and Devices. Mater. Today 2007, 10, 40-48.

52. J.-Y. Chen, C.-L. Hsin, C.-W. Huang, C.-H. Chiu, Y.-T. Huang, S.-J. Lin, W.-W. Wu, L.-J. Chen, Dynamic Evolution of Conducting Nanofilament in Resistive Switching Memories. Nano Lett., 2013, 13 3671–3677.

53. L. Li1, Y. Zhang, Z. Chew, A Cu/ZnO Nanowire/Cu Resistive Switching Device. Nano-Micro Lett. 2013, 5 159-162.

54. Z. Zhang, K. Yao, Y. Liu, C. Jin, X. Liang, Q. Chen, L.-M. Peng, Quantitative Analysis of Current–Voltage Characteristics of Semiconducting Nanowires: Decoupling of Contact Effects. Adv. Funct. Mater. 2007, 17 2478-2489.

55. J. Xiao, W. L. Ong, Z. Guo, G. W. Ho, K. Zeng, Resistive Switching and Polarization Reversal of Hydrothermal-Method-Grown Undoped Zinc Oxide Nanorods by Using Scanning Probe Microscopy Techniques. ACS Appl. Mater. Interfaces 2015, 7 11412-11422.

56. W. Wu, Z. L. Wang, Piezotronic Nanowire-Based Resistive Switches as Programmable Electromechanical Memories. Nano Lett. 2011, 11, 2779-2785.